Antiferromagnetism caused by excess electrons and multiple topological electronic states in the electride $Ba_4Al_5 \cdot e^-$

Weizhen Meng, Xiaoming Zhang,* Ying Liu, Xuefang Dai, and Guodong Liu†
School of Materials Science and Engineering, Hebei University of Technology, Tianjin 300130, China

(Received 20 July 2021; accepted 9 November 2021; published 23 November 2021)

Electrides are a hot research topic due to their special electronic distribution. Recently, the coupling effects among electrides, magnetism, and topological electronic states have attracted considerable attention in condensed-matter physics. Here, based on first-principles calculations, we report an electride phase, namely, $Ba_4Al_5 \cdot e^-$, with combing antiferromagnetic magnetism and multiple types of nontrivial band crossings locating near the Fermi level. The electride feature in $Ba_4Al_5 \cdot e^-$ has been evidenced by electron contribution calculations and symmetry analysis. The material is found to show an antiferromagnetic ground state. Especially, the magnetism in the system is provided by the excess electrons in the crystal cavity, which is fundamentally different from the orbital-composed one in traditional magnetic materials. In addition, near the Fermi level (−0.3 to 0.3 eV) the material shows several regions of band crossings, which are mainly contributed by excess electrons. These band crossings form different topological states, ranging from the zero-dimensional nodal point to the one-dimensional nodal line and two-dimensional nodal surface. The protection mechanism, the effective model, the surface states, and the impacts of spin-orbital coupling on the topological states are systematically discussed. In addition, $Ba_4Al_5 \cdot e^-$ has a very low work function and good catalysis on the [001] surface. Our work provides an excellent candidate for studying the potential entanglement of electride states, magnetism, and nontrivial band topology.

DOI: 10.1103/PhysRevB.104.195145

I. INTRODUCTION

Electrides, as a special kind of material, are different from typical covalent, ion, and intermetallic compounds. That is, the excess electrons are trapped in the crystal cavity as anions and do not participate in bonding [1,2]. Specifically, electrides were first synthesized experimentally in the organic compound $Cs^+(18\text{-crown-}6)_2 \cdot e^-$ [3]. Subsequently, various organic electrides were successfully prepared using different methods [4,5]. Since organic electrides are easily oxidized and hydrolyzed, their physical and chemical properties are difficult to study. However, Matsuishi *et al.* [6] successfully synthesize the zero-dimensional (0D) inorganic electride $Ca_6Al_7O_{16} \cdot e^-$ (C12A7 $\cdot e^-$) with high stability at room temperature. Then, researchers found the electride C12A7$\cdot e^-$ possesses various novel physical and chemical properties, such as higher mobility [6], lower work function [7], low-temperature superconductivity [8], high-efficiency catalysis, etc. [9–11], thus opening a new chapter in the application of inorganic electrides. Afterward, Lee *et al.* [12] predicted a novel two-dimensional (2D) electride, Ca_2N, extending electrides from 0D to 2D. To further enrich the 2D electride family, Inoshita *et al.* [13] and Ming *et al.* [14] determined more 2D electrides using density functional theory (DFT) calculations, such as Y_2C, Gd_2C, Ho_2C, and Dy_2C. After the 2D electrides were reported, the electrides were classified into 0D, one-dimensional (1D), 2D, and three-dimensional (3D) according to the shape of the excess electrons in the crystal cavity. More recently, more inorganic electrides were predicted by high-throughput calculations [13–18], which greatly expanded the electride family.

Recently, due to the expansion of topological insulators to topological semimetals, the classification of topological materials was greatly enriched, including Weyl semimetals [19–22], Dirac semimetals [23–26], nodal line semimetals [27,28], nodal surface semimetals [29,30], etc. However, researchers found that observing the presence of these fermions still faces huge challenges. Interestingly, coupling the topology and the electride to each other is expected to enhance the quantum behavior of topological electrons, thus attracting extensive attention in condensed-matter physics. In fact, in 2018, four teams reported topological features of different electrides, namely, the Dirac point in the 0D electride Ca_3Pb [31], the type-II nodal line in the 2D electride Y_2C [32], the multiple topological behaviors in the electride Sc_2C family [33], and nodal line electrides Os_3O and Ba_5N [34]. In addition, Zhu *et al.* [35] designed novel A_3B-type topological electrides, namely, Rb_3O and K_3O. It is found that in addition to the perfect topological properties of the A_3B-type electrides, there are multiple types of crystal cavities in Rb_3O and K_3O, thus allowing them to possess a high degree of flexibility in excess strain and chemical substitution. The above reports indicate that the coupling of topology and electrides may lead to many peculiar physical properties. However, if topology, magnetism, and electrides are coupled, what novel physical properties do they bring?

*zhangxiaoming87@hebut.edu.cn
†gdliu1978@126.com

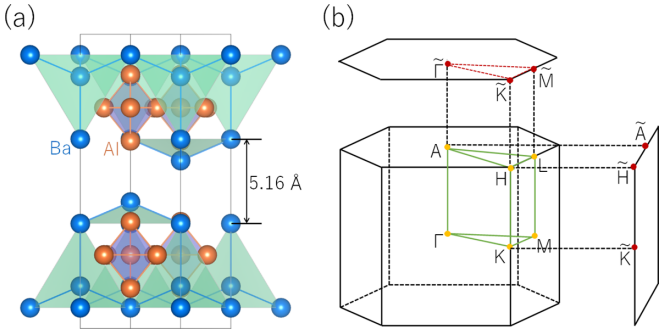

FIG. 1. (a) shows the crystal structure for the electride $Ba_4Al_5 \cdot e^-$. The structure is divided into two layers; layer spacing is 5.16 Å. Blue represents Ba atoms, and yellow represents Al atoms. (b) shows the Brillouin zone for the electride $Ba_4Al_5 \cdot e^-$. The top and side views are the projection surfaces of [001] and [010], respectively.

In this work, based on first-principles calculations and symmetry analysis, we report that the local antiferromagnetic electride $Ba_4Al_5 \cdot e^-$ possesses rich topological states, namely, a triply degenerate nodal point, a Dirac point, Weyl nodal lines, and a nodal surface. Specifically, we first discuss the electride origin using four aspects: the valence state, electron localization function, density of states, and topological quantum chemistry. Afterward, we use a Stoner-type mechanism to explain the magnetic origin and confirm the magnetic ground state of the electride $Ba_4Al_5 \cdot e^-$. We combine DFT calculations and symmetry operations to study the topological states. For example, a TS_z combined operation ensures the formation of the nodal surface. Remarkably, the Fermi arc and drumheadlike surface states of the nodal points and nodal loops are clearly observed. Furthermore, $Ba_4Al_5 \cdot e^-$ has a very low work function and good catalysis on the [001] surface. Finally, we study the electride properties by applying biaxial strain and achieve the local magnetic electrons that will be transformed into itinerant magnetic electrons.

II. CALCULATION METHODS

The first-principles calculations were performed in the framework of DFT by using the Vienna Ab initio Simulation Package (VASP) [36,37] to study the electride, structure, electronic, and magnetic behaviors of the $Ba_4Al_5 \cdot e^-$ compound. For ionic potentials, we used the generalized gradient approximation of the Perdew-Burke-Ernzerhof method [38]. The cutoff energy was adopted as 400 eV, and the Brillouin zone (BZ) was sampled with a Γ-centered k-point mesh of $11 \times 11 \times 11$ for both structural optimization and self-consistent calculations. The energy convergence criteria were chosen to be 10^{-5} eV. The surface states are calculated using Wannier functions [39,40] and the iterative Green's function method [41] as implemented in the WANNIERTOOLS package [42].

III. CRYSTAL STRUCTURE AND ELECTRIDE ORIGIN

The crystal structure for the bulk material Ba_4Al_5 is shown in Fig. 1(a). The compound Ba_4Al_5, with a hexagonal structure, belongs to space group (SG) $P6_3/mmc$ (No. 194), as shown in Fig. 1(b). The lattice constants are $a = b = 6.12$ Å, $c = 17.95$ Å, which are close to the experimental values [43]. The Wyckoff positions of the atoms are Ba_1 [$4f$ (1/3, 2/3, 0.569)], Ba_2 [$4e$ (0, 0, 0.142)], Al_1 [$4f$ (1/3, 2/3, 0.136)], and Al_2 [$6h$ (0.510, 2x, 1/4)]. Among them, a unit cell contains 8 Ba and 10 Al atoms. Interestingly, the atoms of Ba_4Al_5 are divided into two layers; each layer possesses four Ba and five Al atoms, and layer spacing is 5.16 Å. As shown in Fig. 1(a), the Al-Al and Ba-Ba atoms display a regular tetrahedron and octahedron, respectively. Furthermore, these interlinked tetrahedrons and octahedrons form a typical kagome net [see Fig. 1(a)].

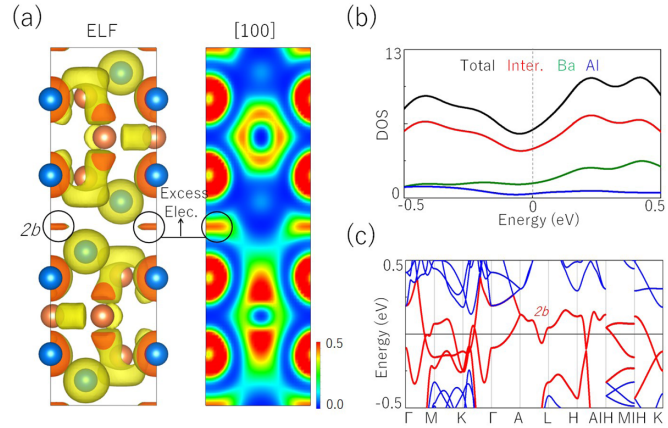

FIG. 2. (a) shows the electron localization function (ELF) for the electride $Ba_4Al_5 \cdot e^-$. The right is a slice of the ELF along the [100] direction. The isosurfaces are plotted at values of 0.6. The black circle shows the excess electrons in the $2b$ site for the electride $Ba_4Al_5 \cdot e^-$. (b) shows density of state (DOS) under nonmagnetic for the electride $Ba_4Al_5 \cdot e^-$. The red curve represents the contribution of interstitial electrons. (c) shows the electronic band structure under the nonmagnetic state. The red band near Fermi level is provided by excess electron in $2b$ site.

Next, the electride origin of Ba_4Al_5 is discussed using four aspects: the valence state (VS), electron localization function (ELF), density of states (DOS), and topological quantum chemistry (TQC) [44]. It is well known that the first requirement to satisfy the electride is that the VS of the compounds is greater than zero. In fact, Jehle *et al.* [43] reported that the VS of Al_5 is -7 (Al_5^{7-}) and the VS of Ba_4 is $+8$ (Ba_4^{8+}) in Ba_4Al_5. Thus, Ba_4Al_5 possesses an excess electron, namely, $Ba_4Al_5 \cdot e^-$. In other words, the excess electrons in $Ba_4Al_5 \cdot e^-$ are supplied by the Ba atoms. The second criterion of the electrides is that there is a large enough crystal cavity in the crystal structure to trap excess electrons [31]. The existence of a big layer space in $Ba_4Al_5 \cdot e^-$ is shown in Fig. 1(a). To confirm that the excess electrons are, indeed, trapped by the lattice cavity, we draw an ELF map of $Ba_4Al_5 \cdot e^-$, as shown in Fig. 2(a). In addition to the orbital electrons around the Ba and Al atoms, we do find that excess electrons are trapped in the layer space (namely, the $2b$ site). Third, for electrides, the bands near the Fermi level are mainly contributed by excess electrons [7]. Here, we calculate the DOS of $Ba_4Al_5 \cdot e^-$, as shown in Fig. 2(b). The DOS shows that the band near the Fermi level is filled with more interstitial electrons. To put it another way, the excess electrons are mainly involved in the conductive behavior in $Ba_4Al_5 \cdot e^-$. More recently, Nie

et al. [45] proposed the application of TQC theory to electrides. They found that band representations (BRs) near the Fermi level in electrides are contributed by excess electrons in the crystal cavity. Using the programs IRVSP and POS2ABR [46,47], we calculate that the BRs near the Fermi level (−0.3 to 0.3 eV) in $Ba_4Al_5 \cdot e^-$ are 2*b*@*A/B/E* (2*b* represents the Wyckoff position, and *A/B/E* are the irreducible representations of the band), which means that the band near the Fermi level comes from the interstitial electrons rather than from the orbital electrons. The above results indicate that $Ba_4Al_5 \cdot e^-$ is a typical 0D electride.

IV. ORIGIN OF LOCAL MAGNETISM

The magnetic moments of previously reported magnetic electrides are mainly provided by orbital electrons around atoms [48,49]. In fact, the isolated excess electrons also may be the origin of magnetism. Here, based on the DFT calculations, we find that the 0D electride $Ba_4Al_5 \cdot e^-$ produces spin splitting, and the magnetic moment comes from the excess electrons in the 2*b* site. Next, we use the Stoner-type instability [50] to explain its magnetic origin. Specifically, when the compounds with itinerant electrons are satisfied by $D(E_f) \times I > 1$ [where $D(E_f)$ is the value of the DOS in E_f and I is the effective exchange interaction parameter), the ferromagnetic (FM) ground state is very likely to form in these compounds. It is well known that the parameter I is suitable for only the exchange interaction of orbital electrons around atoms. For the electride $Ba_4Al_5 \cdot e^-$, although it is difficult to deal with isolated excess electrons' exchange interaction, the value of I in all electrides is likely to be consistent due to isolated excess electrons with *s*-like features [51]. Therefore, $D(E_f)$ will play a very important role in electrides.

Previously, the Stoner-type instability was applied to explain the appearance of magnetism in high-pressure alkali-metal electrides [52]. Recently, it was argued that the distribution and degree of quantum confinement of excess electrons at the Fermi level are a potential indicator of the degree of electron dispersion and stoner instability [53,54]. This view is reasonable in the ideal condition that the excess electrons are completely confined to the lattice cavity. For the electride Ba_4Al_5, the DOSs displayed in Fig. 2(b) show that the states near the Fermi level are mainly contributed by the excess electrons, but there are still some orbital electrons involved. The hybridization between the excess electrons and the orbital electrons may weaken the DOS peak at the Fermi level. However, we note that the orbital states near the Fermi level are significantly fewer than those from excess electrons [see Fig. 2(b)]. For this consideration, we still evaluate the Stoner-type instability in the electride Ba_4Al_5. As shown in Fig. 3, we find that the DOS at the Fermi level for the nonmagnetic (NM) state situates at a peak (with a value of 17.1 electrons/eV), which is significantly larger than that for the magnetic state. These results suggest the Stoner-type instability may also apply to Ba_4Al_5.

Next, we discuss the magnetic ground state of the electride $Ba_4Al_5 \cdot e^-$. Remarkably, the isolated excess electrons do not belong to any atoms, but Kim *et al.* [55] proposed that assigning the magnetic moment to the cation closest to the isolated excess electrons is the best way to calculate organic

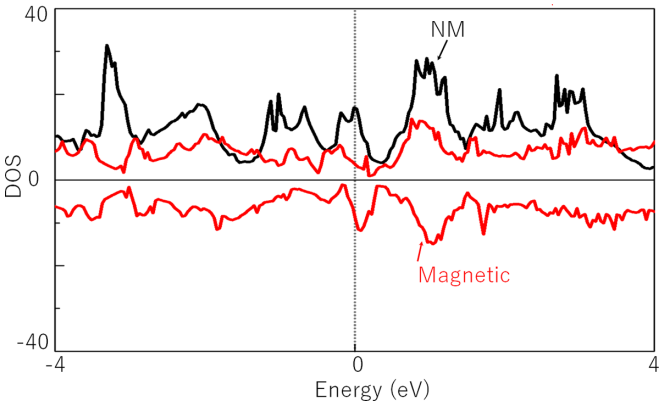

FIG. 3. The total DOS under nonmagnetic (NM) and magnetic states for the electride $Ba_4Al_5 \cdot e^-$.

magnetic electrides. For the inorganic electride $Ba_4Al_5 \cdot e^-$, the cations closest to the isolated excess electrons are the Ba atoms on the four edges. Therefore, we consider four magnetic ground states: FM and antiferromagnetic (AFM1, AFM2, and AFM3), as shown in Fig. 4(a). The results show that AFM2 possesses the lowest energy, as shown in Fig. 4(b). Based on the DFT calculation, Ba and Al atoms provide a weak magnetic moment ($0.025\mu_B$), and the interstitial electrons provide the main magnetic moment (about $0.83\mu_B$). Therefore, we need to consider only the magnetic exchange coupling of the excess electrons. Here, we consider three magnetic exchange couplings of excess electrons, as shown in Fig. 4(b). We use the effective Heisenberg model $\widehat{H} = \sum_{ij} J_{ij}\widehat{S}_i\widehat{S}_j$ to calculate the exchange coupling J between adjacent excess electrons at different positions (J_1, J_2, J_3), as shown in Fig. 4(b). The

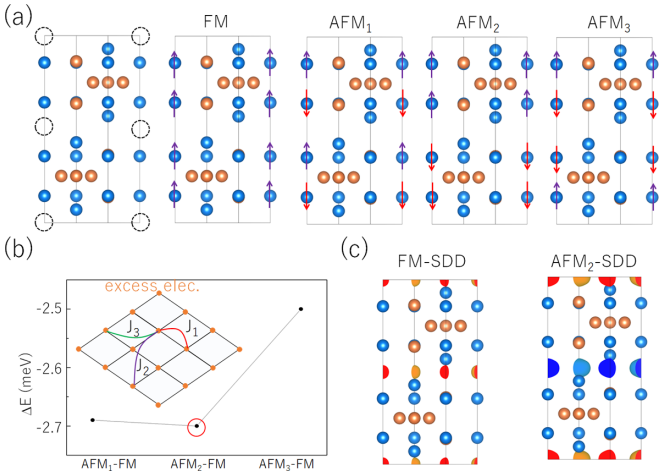

FIG. 4. (a) shows the four magnetic configurations for the electride $Ba_4Al_5 \cdot e^-$: ferromagnetic (FM) and antiferromagnetic (AFM1, AFM2, and AFM3). The purple and red arrows represent spin up and spin down, respectively. (b) The energy value change curve under the above magnetic configurations. Among them, AFM2 is the final magnetic ground state for $Ba_4Al_5 \cdot e^-$. The illustration shows the direct exchange of excess electrons, namely, J_1, J_2, and J_3. (c) shows the spin difference density (SDD) under FM and AFM2. The isosurface is at $0.0025\mu_B/\text{Å}^3$; the yellow and blue charges represent spin up and spin down, respectively.

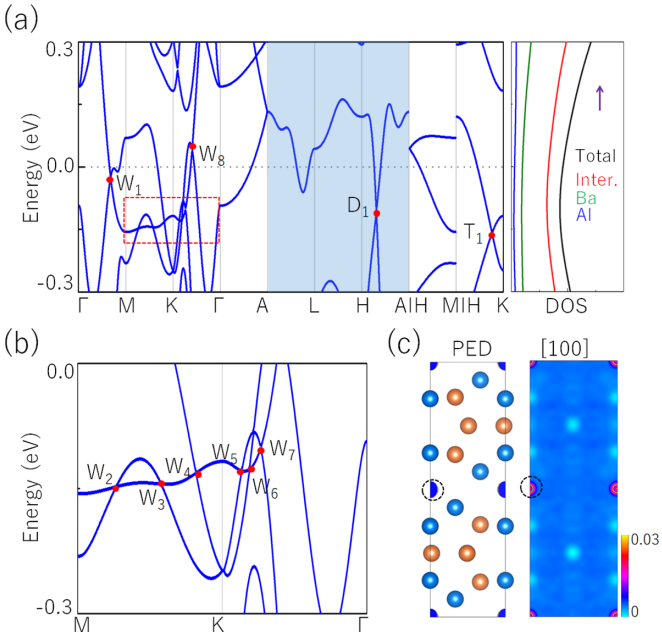

FIG. 5. (a) shows the electronic band structure without SOC and the DOS of the spin-up channel for the electride $Ba_4Al_5 \cdot e^-$. In the DOS plot, the red line represents the density of states contributed by interspace electrons. (b) shows the locally enlarged band of the red box in (a). In (a) and (b), all crossing points are denoted as W_{1-8}, D_1, and T_1. (c) shows the partial charge density (PCD) near the Fermi level (−0.3 to 0.3 eV); the isosurface is at 0.003 e/Å^3. The right part is a slice of the PCD along the [100] direction.

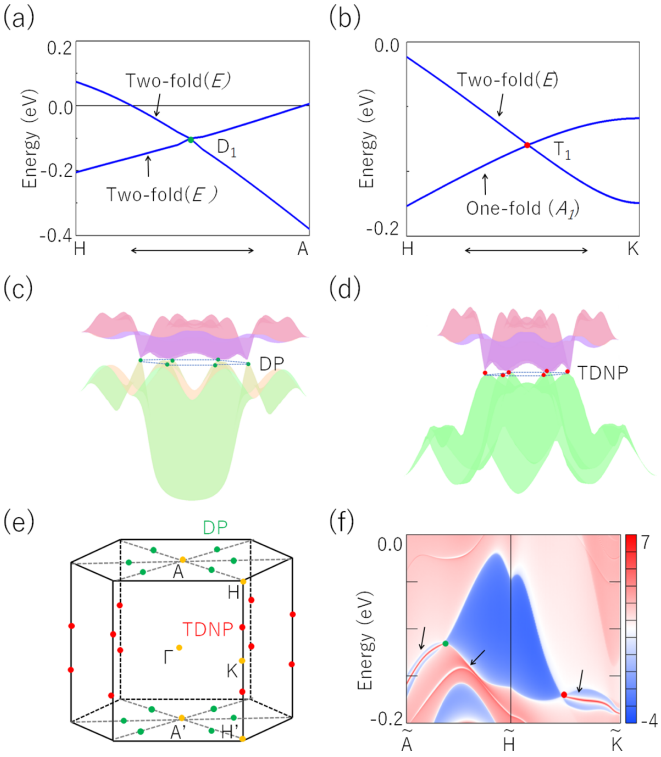

FIG. 6. (a) and (b) show the enlarged band around D_1 and T_1 for the electride $Ba_4Al_5 \cdot e^-$; E and A_1 represent irreducible representations. (c) and (d) show the 3D dispersion bands of D_1 and T_1, respectively. (e) shows the positions of D_1 and T_1 in the BZ. (f) shows the surface states of D_1 and T_1 on the [010] plane. The black arrows point to Fermi arc surface states.

magnetic moments used in the effective Heisenberg model are the results from the DFT calculation. The values of J_1, J_2, and J_3 are −17, −4.2, and −7.43 meV, which show that the antiferromagnetic arrangement of magnetic moments is preferred. Furthermore, it is also obvious that the magnetic exchange coupling J_1 is significantly greater than the others, J_2 and J_3. As shown in Fig. 4(b), the magnetic exchange coupling J_1 is the nearest neighbor in this quadrilateral plane and has sufficient small atomic space, which leads to the stronger exchange interaction. In addition, we calculate the spin difference density (SDD) of the electride $Ba_4Al_5 \cdot e^-$, as shown in Fig. 4(c). Although we apply the magnetic moment to Ba atoms, the SDD shows that the magnetic moment is still provided by the isolated excess electrons, which agrees well with the results of our previous analysis.

V. 0D, 1D, AND 2D BAND CROSSINGS IN THE ELECTRONIC STRUCTURE

Before studying the topological features, let us discuss the electronic structure of the electride $Ba_4Al_5 \cdot e^-$. Figure 5(a) shows the electronic band structure without considering spin-orbit coupling (SOC). We find that the spin-up bands and the spin-down bands are completely degenerate, and two bands pass through the Fermi level, showing typical magnetic metal features. In addition, the DOS shows that the bands near the Fermi level are mainly contributed by interstitial excess electrons, as shown in Fig. 5(a). Also, the partial charge density (PCD) indicates that the bands in the energy range of −0.3 to 0.3 eV are also mainly provided by excess electrons in the 2*b* site, as shown in Fig. 5(c). This means that more of the electrons involved in conducting electricity come from the excess electrons of lattice cavities (namely, the 2*b* site). Remarkably, we find 10 crossing points (CPs) on k paths Γ-*M*-*K*-Γ and *A*-*H*-*K*, denoted as W_{1-8}, D_1, and T_1, respectively. Furthermore, there is a twofold-degenerate band along k paths *A*-*L*-*H*-*A*, as shown in Figs. 5(a) and 5(b). Next, we will discuss the topological features of these CPs in the electride $Ba_4Al_5 \cdot e^-$.

Nodal points. First, we focus on the CPs (namely, D_1 and T_1) on k paths *A*-*H*-*K*, as shown in Figs. 6(a) and 6(b). Two doubly degenerate bands with the same irreducible representation E form D_1 on k path *A*-*H*, namely, the Dirac point (DP) [see Fig. 6(a)]. Based on symmetry analysis, this DP is protected by $C_{2(1,-1,0)} = \{x, y, z\} \rightarrow \{-y, -x, -z + 1/2\}$ symmetry. Due to the presence of mirror symmetries, there are six pairs of DPs in the BZ, as shown in Figs 6(c) and 6(e). Furthermore, when making an orbital projection for the band along k path *A*-*H* on the [010] surface, we find two clear nontrivial Fermi arc surface states emanating from the DP, as shown by the green dot in Fig. 6(f). Next, we study the CP T_1 on k path *H*-*K*, as shown in Fig. 6(b). SG 194 contains the symmetry operation $C_{3v} = \{x, y, z\} \rightarrow \{-x + y, -x, z\}$. k path *H*-*K* allows the doubly degenerate band and singly degenerate band to appear due to the existence of symmetry operations C_{3v}. Using the calculations from IRVSP [46], the

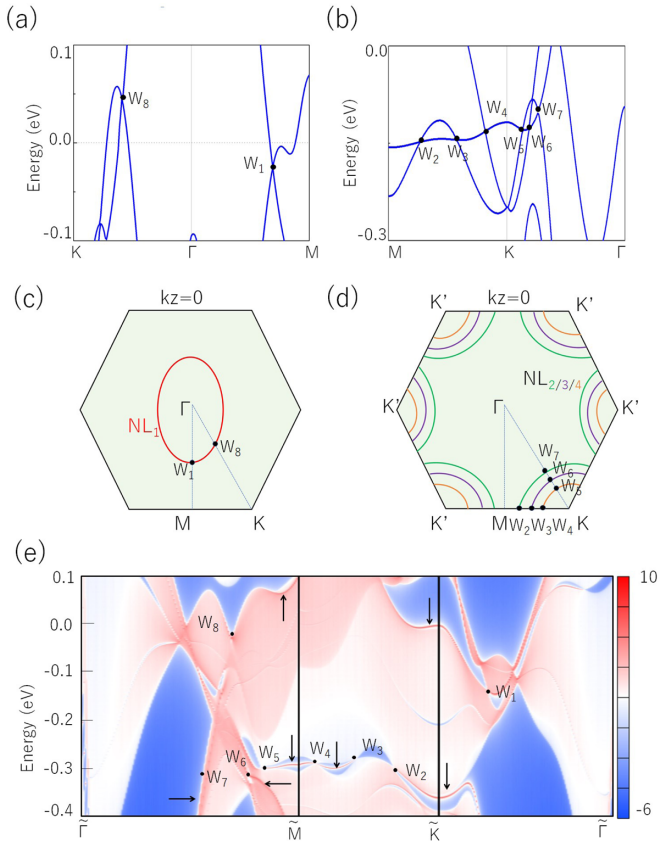

FIG. 7. (a) and (b) show the enlarged band along k paths Γ-M-K-Γ for the electride $Ba_4Al_5 \cdot e^-$. (c) and (d) show the positions of nodal loops (NL_{1-4}) around Γ and K. (e) shows the surface states of these nodal loops on the [001] plane. The arrows point to drumheadlike surface states.

onefold- and twofold- degenerate bands with different irreducible representations (E and A_1) cross to form six pairs of T_1 [namely, the triply degenerate nodal point (TDNP)], as shown in Figs. 6(d) and 6(e). We also construct an orbital projection of the TDNP on k path H-K. The result shows that the TDNP also appears in a nontrivial Fermi arc surface state, as shown by the red dot in Fig. 6(f).

Nodal loops. Before discussing the CPs (namely, W_{1-8}) on k paths Γ-M-K-Γ [see Figs. 7(a) and 7(b)], we first analyze the symmetry operations in the electride $Ba_4Al_5 \cdot e^-$, which contains $M_z = \{x, y, z\} \rightarrow \{x, y, -z + 1/2\}$ and inversion I symmetries. When only considering a single spin direction, the T symmetry will be preserved. We find W_{1-8} are formed by four singly degenerate bands, namely, Weyl points [see Figs. 7(a) and 7(b)]. Because of the existence of IT symmetries [56] in the electride $Ba_4Al_5 \cdot e^-$, these Weyl points should belong to nodal loops (NLs). By DFT calculations, W_1 and W_8 form NL_1 around Γ; W_{2-7} form $NL_{2/3/4}$ around K [see Figs. 7(c) and 7(d)], which agrees well with the results of the symmetry analysis. Since NL_{1-4} are all located on the $k_z = 0$ plane, we take NL_1 around the k-point Γ as an example for more detailed research. Specifically, the irreducible representations of two bands forming NL_1 around Γ are A_{1g} and B_{1u}, which belong to the D_{6h} point group. Based on the above symmetry analysis, the constraints can be written as

$$C_{6z} = \sigma_z, \quad M_x = \sigma_z, \quad M_z = \sigma_0, \quad I = \sigma_z, \quad T = \sigma_0 K. \tag{1}$$

Here, K is the complex conjugation. Under the constrains from these operations,

$$C_{6z}\mathcal{H}(\boldsymbol{k})C_{6z}^{-1} = \mathcal{H}\Big(\cos\frac{\pi}{3}k_x - \sin\frac{\pi}{3}k_y, \cos\frac{\pi}{3}k_x + \sin\frac{\pi}{3}k_y, k_z\Big), \tag{2}$$

$$M_x\mathcal{H}(\boldsymbol{k})M_x^{-1} = \mathcal{H}(-k_x, k_y, k_z), \tag{3}$$

$$M_z\mathcal{H}(\boldsymbol{k})M_z^{-1} = \mathcal{H}(k_x, k_y, -k_z), \tag{4}$$

$$I\mathcal{H}(\boldsymbol{k})I^{-1} = \mathcal{H}(-k_x, -k_y, -k_z), \tag{5}$$

$$T\mathcal{H}(\boldsymbol{k})T^{-1} = \mathcal{H}(-k_x, -k_y, -k_z). \tag{6}$$

Then, the effective Hamiltonian can be written as

$$\mathcal{H}(\boldsymbol{k}) = a(\boldsymbol{k})\sigma_0 + w(\boldsymbol{k})\sigma_z + g(\boldsymbol{k})\sigma_z, \tag{7}$$

$$a(\boldsymbol{k}) = M_0 + \alpha(k_x^2 + k_y^2) + B_0 k_z^2,$$
$$w(\boldsymbol{k}) = \beta\big(k_x^2 + k_y^2 - k_0^2\big),$$
$$g(\boldsymbol{k}) = B_1 k_z^2. \tag{8}$$

Here, σ_0 represents the 2×2 identical matrix, and σ represent the Pauli matrix; k_0 represents the radius of the nodal loop, and α and β represent material-specific parameters. Therefore, the two bands on the $k_z = \pi$ plane form a NL around the Γ point, which completely agrees with the DFT results.

In addition, a typical feature of a NL is the drumheadlike surface states [29,30]. We make an orbital projection on the [001] surface using WANNIERTOOLS [42], drawing the surface spectrum for the electride $Ba_4Al_5 \cdot e^-$, as shown in Fig. 7(e). We do see the drumhead surface states coming out of the NLs, which indicates the nontrivial topology of NLs. Remarkably, the drumheadlike surface states are very clear, which will easily be observed using angle-resolved photoemission spectroscopy (ARPES).

Nodal surface. Next, let us turn to the doubly degenerate band along k paths A-L-H-A on the $k_z = \pi$ plane, as shown in Fig. 8(a). The doubly degenerate band on the $k_z = \pi$ plane may be part of the nodal surface (NS). Based on DFT calculations, the k path L-H is divided into four equal parts, denoted as a, b, c, and d. We calculate the electronic band structure along k paths A-a, A-b, A-c, and A-d, respectively [see Figs. 8(b) and 8(c)]. The result shows the bands of each k path are all twofold degenerate. Furthermore, we also calculate the 3D dispersion band on the $k_z = \pi$ plane, as shown in Fig. 8(d). The result shows the valence band and conduction band are completely degenerate on the entire $k_z = \pi$ plane. The above results confirm that the bands on the $k_z = \pi$ plane are NSs.

To further ensure that bands on the $k_z = \pi$ plane are NSs, we discuss them in more detail using symmetry. Generally, the NS is protected by two combined symmetries, namely, T and the screw rotation operation. It is well known that there is no T symmetry in magnetic systems. For the electride $Ba_4Al_5 \cdot e^-$,

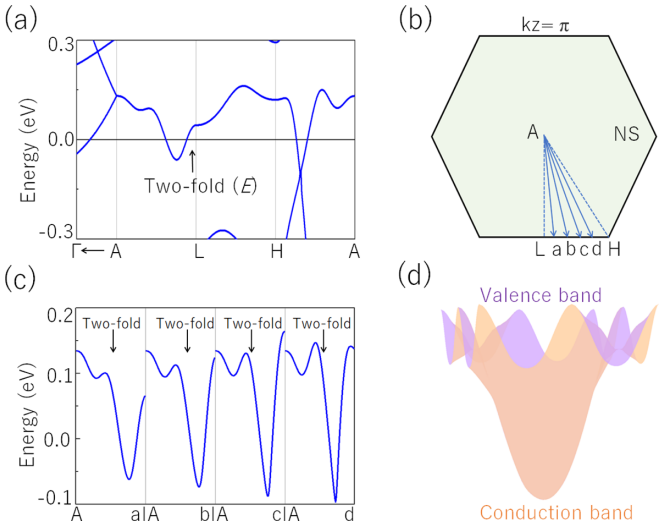

FIG. 8. (a) shows the electronic band structure along the k paths A-L-H-A for the electride $Ba_4Al_5 \cdot e^-$. (b) shows the $k_z = \pi$ plane; the k path L-H is divided into four equal parts, denoted as a, b, c, and d. (c) The electronic band structure along k paths A-a, A-b, A-c, and A-d. The bands on each path all are twofold degenerate. (d) shows the 3D dispersion bands of nodal surface.

if only a single spin channel is considered, the T symmetry will be preserved. In addition, this system indeed contains a screw rotation operation, $S_z = \{x, y, z\} \rightarrow \{-x, -y, z + 1/2\}$. When two symmetries ($TS_z$) combined operate on the invariant space $k_z = \pi$ plane,

$$(TS_z) = T_{001} = e^{-ik_z} = -1. \tag{9}$$

This means the twofold-degenerate band will form on the entire $k_z = \pi$ plane, which agrees well with the DFT results.

SOC effect. Before discussing the electronic band structure under SOC, we first need to know the easy magnetization direction for the electride $Ba_4Al_5 \cdot e^-$. Here, we consider four magnetization directions, namely, [001], [010], [100], and [110]. The result shows [010] has the lowest energy, as shown in Figs. 9(a) and 9(b). Then, we calculate the electronic band structure along the [010] easy magnetization direction, as shown in Fig. 9(c). Based on symmetry analysis, when the magnetic moment is applied to the [010] direction, the S_z, M_z, and C_{3v} symmetries are broken. This means that the DP, TDNP, NLs, and NS will disappear under the [010] magnetization direction, and new fermions may form. Specifically, the DP and TDNP open tiny gaps (about 26.9 and 19 meV), forming Weyl points (WP_{1-3}) [see Figs. 9(c) and 9(d)].$WP_{1,2}$ and WP_3 are protected by $M_{(1-10)}$ and $M_{(010)}$ symmetries, respectively. Furthermore, all NLs are broken, opening tiny energy gaps, namely, 22, 11, 9.8, 5.1, 0.8, 1.2, 24, and 9 meV [see Figs. 9(c) and 9(d)]. These energy gaps are very close to those of previous typical nodal line semimetals, such as Cu_3NPd (60–100 meV) [57], CaAgBi (80–140 meV) [58], and $BaSn_2$ (60–160 meV) [59]. The doubly degenerate band along the k paths A-L-H-A produces a split, but the nodal line on k path A-L is preserved, as shown in Figs. 9(c) and 9(d). Figure 9(e) shows the positions of the WPs and NL in the BZ under SOC. The above results show that $Ba_4Al_5 \cdot e^-$ is also an excellent electride for studying WPs and NLs under SOC.

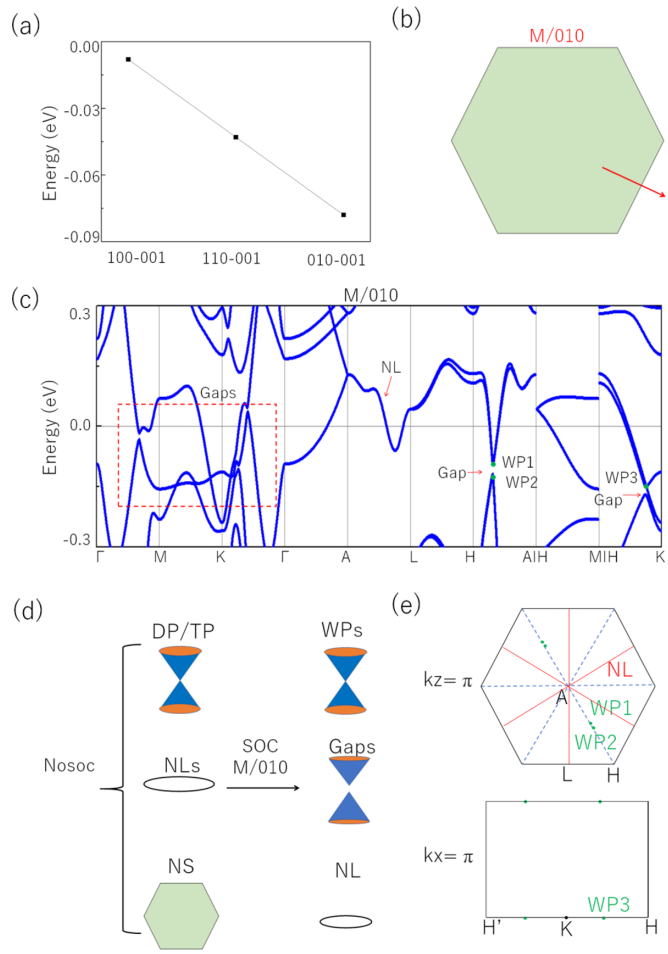

FIG. 9. (a) shows the energy values of the magnetic moment along four directions under SOC for the electride $Ba_4Al_5 \cdot e^-$, namely, [001], [010], [100], and [110]. (b) shows [010] is the easy magnetization direction. (c) shows the electronic band structure along the [001] easy magnetization direction under SOC. Three crossing points and a doubly degenerate band exist on k paths A-H-K and A-L, respectively. (d) The Dirac point (DP), triply degenerate nodal point (TDNP), and nodal loops (NLs) and nodal surface (NS) are transformed into Weyl points (WPs), tiny gaps, and a NL under SOC, respectively. (e) shows the positions of these fermions in the BZ, namely, WP_{1-3} and NL.

VI. DISCUSSION AND CONCLUSION

The above results show Ba_4Al_5 is a special material which combines the features of electrides, magnetism, and a topologically nontrivial electronic structure. With these features combined together, here, we argue that two unique properties can be expected in Ba_4Al_5. The first one is the relatively low work function with high electron mobility, brought by the effects of combining the electride, magnetism, and nontrivial band topology. It is well known that the excess electrons in electrides neither belong to atoms nor participate in bonding but are bound in a lattice cavity as anions. Therefore, electrides tend to possess a very low work function. In addition, magnetism in materials is also believed to be a factor which can lower the work function [60,61]. In Ba_4Al_5, as shown in Figs. 10(a) and 10(b), we compare the work function on the

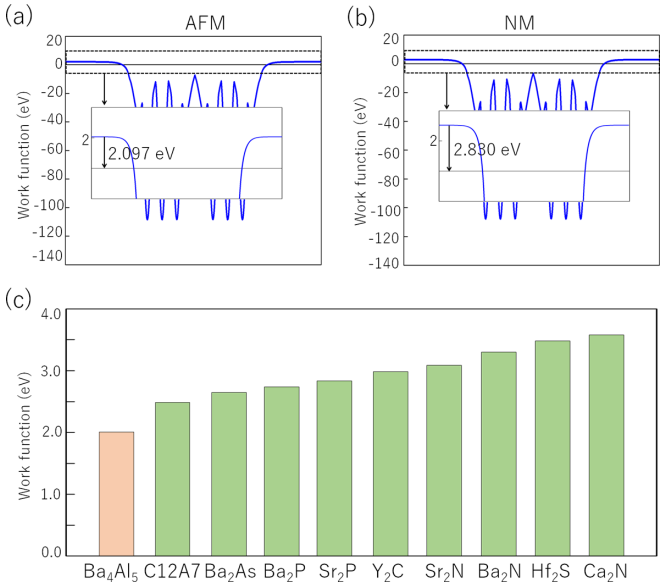

FIG. 10. (a) and (b) The work function (WF) of the electride Ba_4Al_5 on the [001] surface under AFM and NM states, respectively. In (a) and (b), the illustrations are partial enlargements. (c) Comparison of work functions between AFM Ba_4Al_5 and other NM electrides.

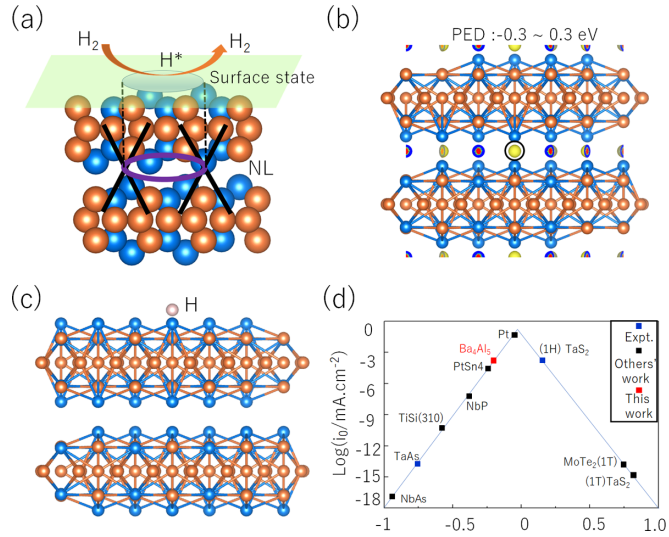

FIG. 11. (a) The hydrogen evolution reaction (HER) process for the electride Ba_4Al_5; the drumhead surface states induced by the nodal line states activate the [001] surface for the HER. (b) shows the partial charge density at -0.3 to 0.3 eV for supercell ($3 \times 3 \times 1$) Ba_4Al_5; the circle represents the excess electrons. The isosurface value is chosen to be 0.0035 $bohr^{-3}$. (c) shows the final structure for H adsorbed on the [001] surface of Ba_4Al_5. (d) Volcano plot for HER of Ba_4Al_5 in comparison with typical catalysts. The data are taken from Refs. [65,66].

[001] surface between the AFM and NM states, which shows the work function under the AFM state is about 0.8 eV lower than that under the NM state in Ba_4Al_5. The results show that magnetism may act as a way to further lower the work function in electrides. In addition, we have compared the work function between AFM Ba_4Al_5 and typical NM electrides, and the results are shown Fig. 10(c). We find that the work function in Ba_4Al_5 (2.09 eV) is lower than in typical NM electrides, including C12A7 (2.4 eV) [7], Ca_2N (3.5 eV) [12], Y_2C (2.9 eV) [62], Sr_2N (3.19 eV), Ba_2N (3.39 eV), Ba_2As (2.58 eV), Ba_2P (2.66 eV), Sr_2P (2.8 eV) [14], and Hf_2S (3.4 eV) [63]. The relatively low work function in Ba_4Al_5 makes it a candidate for electronic applications such as efficient thermionic emitters. For electron emissions, besides the work function, the carrier mobility is another important parameter. In Ba_4Al_5, it shows topological band crossings contributed by the excess electronic states near the Fermi level. These band crossings exhibit linear band dispersions, which naturally have high carrier mobility. Thus, by combing the electride, magnetism, and topological band crossings, Ba_4Al_5 is expected to have a relatively low work function with high electron mobility.

For the second property, we find the coupling between the electride feature and topologically nontrivial electronic structures makes Ba_4Al_5 promising as a high-performance catalyst for the hydrogen evolution reaction (HER). In electrides, the excess electrons are loosely bounded and are believed to favor the catalytic process for various reactions [9–11]. Ba_4Al_5 also contains excess electrons. However, unlike traditional electrides, the excess electrons in Ba_4Al_5 can contribute the nontrivial band crossings (see Fig. 5). These band crossings (especially the nodal line) produce nontrivial surface states on the surface [see Figs. 6, 7, and 11(a)]. The nontrivial surface states are also expected to favor the catalytic performance, which was proposed in topological insulators and various topological semimetals [64–67]. Unlike traditional topological materials, the topological fermions in Ba_4Al_5 combine with the electride feature, which may further enhance the catalytic ability. We have evaluated the catalytic ability for HER in Ba_4Al_5 by calculating the Gibbs free energy on the [001] surface. We find the hydrogen atom tends to be adsorbed above the site with excess electrons in Ba_4Al_5, as shown in Figs. 11(b) and 11(c). As a result, the calculated Gibbs free energy for HER in Ba_4Al_5 is only 0.217 eV, which is smaller than in traditional Weyl semimetals in the TaAs family [65], as shown in Fig. 11(d). These results suggest electrides with nontrivial topology are promising for high-performance catalysts.

Furthermore, we observe the continuous change process of excess electrons in the electride Ba_4Al_5 by applying different biaxial strains. As shown in Fig. 12(a), when we apply tension strain (0%–8%) along the z axis, the lattice cavity of the $2b$ site becomes even more spacious due to lattice expansion along the z direction. Compared with the condition without strain, with the increase of tensile strain, the active radius of electrons in the lattice cavity is larger, making the degree of electron localization better [see Fig. 12(a)]. The better the degree of electronic localization is, the more advantageous the application of electronic crystals in electronic devices may be. After we apply different compression strains along the z axis (0% to -8%), the $2b$ site of the lattice cavity gradually decreases due to the lattice shrinkage in the z direction (namely, the lattice expansion along the x/y directions) [see Fig. 12(b)]. We observe that the accumulation of excess electrons in the lattice

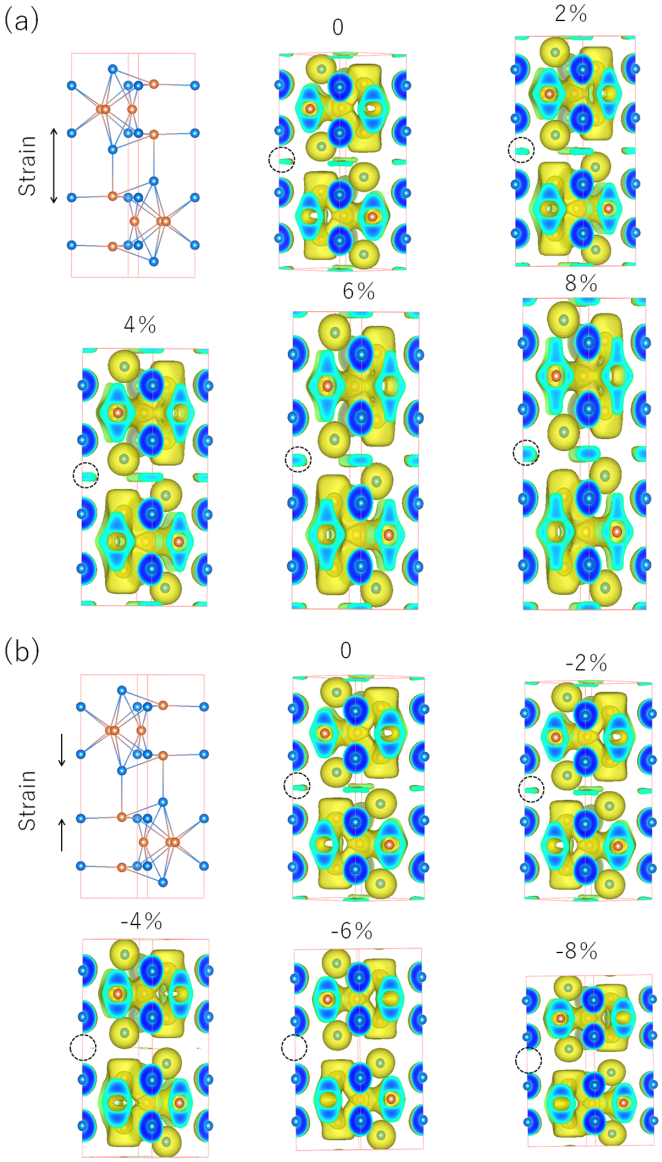

FIG. 12. (a) and (b) show the continuous change process of excess electrons in the electride $Ba_4Al_5 \cdot e^-$ by applying different biaxial strains. The dotted boxes represent excess electrons in the 2*b* site.

cavity 2*b* site gradually decreases. When the compression strain reaches above 6% [$> -6\%$; see Fig 12(b)], the lattice cavity is not capable of capturing excess electrons, which causes the original local electrons to be transformed into itinerant electrons. Therefore, we cause the local magnetic electrons to be transformed into itinerant magnetic electrons by applying biaxial strain.

Finally, we find that coupled magnetism, topological states and electron crystals can bring new physical properties to the electride Ba_4Al_5. (1) It is well known that most of the magnetic origin of electrides comes from orbital electrons [48,49]. In fact, excess electrons in the crystal cavity can also produce spin splitting. Especially, reports of local AFM electrides are relatively rare. (2) A single electride usually contains only one topological state in previous works [31,32,34]. The electride Ba_4Al_5 contains three types of fermions, namely, 0D (DP and TDNP), 1D (NLs) and 2D (NS), thus providing an excellent material to study the potential entanglement of the above fermions. (3) Unlike the usual topological materials, the bands near the Fermi energy level are mainly contributed by the excess electrons of the crystal cavity rather than orbital electrons in the electride Ba_4Al_5. (4) For the electride Ba_4Al_5, although the bands near the Fermi level (-0.3 to 0.3) are relatively complex, the surface states corresponding to these fermions are extremely clear, which will facilitate future observations by ARPES.

In conclusion, we reported a local antiferromagnetic electride, $Ba_4Al_5 \cdot e^-$, with multiple types of topological states. Specifically, we confirmed the origin of excess electrons in the crystal cavity using different methods. Then, the interstitial magnetic source and antiferromagnetic ground state were determined based on the Stoner type. We found that the electride $Ba_4Al_5 \cdot e^-$ possesses several nontrivial band crossings near the Fermi level under the antiferromagnetic ground state. These band crossings form the Dirac point, triply degenerate nodal point, nodal loops, and nodal surface. Remarkably, different from previous topological materials, these fermions are all contributed by excess electrons in the crystal cavity. Furthermore, these fermions show strong robustness without SOC due to the protection of the symmetries. When the SOC is not ignored, these fermions translate into the Weyl point and nodal line. Finally, we caused the local electrons to be transformed into itinerant electrons by applying biaxial strain. Therefore, we provide an excellent candidate material to study the coupling among topology, magnetism, and electrides.

ACKNOWLEDGMENTS

This work is supported by the National Natural Science Foundation of China (Grant No. 11904074). This work is funded by the Science and Technology Project of the Hebei Education Department, the Nature Science Foundation of Hebei Province, the S&T Program of Hebei (Grants No. A2019202107 and No. A2021202012), the Overseas Scientists Sponsorship Program of Hebei Province (Grant No. C20210330), and the Hebei University of Technology. X.Z. acknowledges the financial support from the Young Elite Scientists Sponsorship Program of Tianjin.

[1] J. L. Dye, Nature (London) **365**, 10 (1993).
[2] Z. Li, J. Yang, J. Hou, Q. Zhu, J. Am. Chem. Soc. **125**, 6050 (2003).
[3] S. B. Dawes, D. L. Ward, R. H. Huang, and J. L. Dye, J. Am. Chem. Soc. **108**, 3534 (1986).
[4] R. Haung, M. Faber, K. Moeggenborg, D. Ward, and J. Dye, Nature (London) **331**, 599 (1988).
[5] R. Rencsok, T. Kaplan, and J. Harrison, J. Chem. Phys. **98**, 9758 (1993).
[6] S. Matsuishi, Y. Toda, M. Miyakawa, K. Hayashi, T. Kamiya, M. Hirano, I. Tanaka, and H. Hosono, Science **301**, 626 (2003).

[7] Y. Toda, H. Yanagi, E. Ikenaga, J. J. Kim, M. Kobata, S. Ueda, T. Kamiya, M. Hirano, K. Kobayashi, and H. Hosono, Adv. Mater. **19**, 3564 (2007).

[8] M. Miyakawa, S. W. Kim, M. Hirano, Y. Kohama, H. Kawaji *et al.*, J. Am. Chem. Soc. **129**, 7270 (2007).

[9] M. Kitano, Y. Inoue, Y. Yamazaki, F. Hayashi, S. Kanbara *et al.*, Nat. Chem. **4**, 934 (2012).

[10] Y. Toda, H. Hirayama, N. Kuganathan, A. Torrisi, P. V. Sushko, and H. Hosono, Nat. Commun. **4**, 2378 (2013).

[11] M. Kitano, S. Kanbara, Y. Inoue, N. Kuganathan, and P. V. Sushko, Nat. Commun. **6**, 6731 (2015).

[12] K. Lee, S. W. Kim, Y. Toda, S. Matsuishi, and H. Hosono, Nature (London) **494**, 336 (2013).

[13] T. Inoshita, S. Jeong, N. Hamada, and H. Hosono, Phys. Rev. X **4**, 031023 (2014).

[14] W. M. Ming, M. Yoon, M.-H. Du, K. Lee, and S. W. Kim, J. Am. Chem. Soc. **138**, 15336 (2016).

[15] Y. Zhang, H. Wang, Y. Wang, L. Zhang, Y. Ma, Phys. Rev. X **7**, 011017 (2017).

[16] Q. Zhu, T. Frolov, and K. Choudhary, Matter **1**, 1293 (2019).

[17] X. Yang, K. Parrish, Y.-L. Li, B. Sa, H. Zhan, and Q. Zhu, Phys. Rev. B **103**, 125103 (2021).

[18] T. Yu, M. Hirayama, J. A. Flores-Livas, M.-T. Huebsch, T. Nomoto, and R. Arita, Phys. Rev. Mater. **5**, 044203 (2021).

[19] W. Z. Meng, X. M. Zhang, T. L. He, L. Jin *et al.*, J. Adv. Res. **24**, 523 (2020).

[20] A. A. Soluyanov, D. Gresch, Z. J. Wang, Q. S. Wu, M. Troyer *et al.*, Nature (London) **527**, 495 (2015).

[21] L. Wang, L. Jin, G. Liu, Y. Liu, X. Dai, and X. Zhang, Appl. Mater. Today **23**, 101057 (2021).

[22] T. He, X. Zhang, Y. Liu, X. Dai, G. Liu, Z.-M. Yu, and Y. Yao, Phys. Rev. B **102**, 075133 (2020).

[23] B. J. Wieder, Z. J. Wang, J. Cano, X. Dai, L. M. Schoop, B. Bradlyn, and B. A. Bernevig, Nat. Commun. **11**, 627 (2020).

[24] B. J. Wieder, Y. Kim, A. M. Rappe, and C. L. Kane, Phys. Rev. Lett. **116**, 186402 (2016).

[25] M. Z. Yan, H. Q. Huang, K. N. Zhang, E. Y. Wang, W. Yao, K. Deng, G. L. Wan *et al.*, Nat. Commun. **8**, 257 (2017).

[26] W. Z. Meng, X. M. Zhang, Y. Liu, X. F. Dai, and G. D. Liu, New J. Phys. **22**, 073061 (2020).

[27] T. He, X. Zhang, L. Wang, Y. Liu, X. Dai, L. Wang, and G. Liu, Mater. Today Phys. **17**, 100360 (2021).

[28] L. Jin, X. Zhang, Y. Liu, X. Dai, X. Shen, L. Wang, and G. Liu, Phys. Rev. B **102**, 125118 (2020).

[29] W. K. Wu, Y. Liu, S. Li, C. Y. Zhong, Z. M. Yu, X. L. Sheng, Y. X. Zhao, and S. Y. A. Yang, Phys. Rev. B **97**, 115125 (2018).

[30] B. B. Fu, C. J. Yi, T. T. Zhang, M. Caputo, J. Z. Ma, X. Gao *et al.*, Sci. Adv. **5**, eaau6459 (2019).

[31] X. Zhang, R. Guo, L. Jin, X. F. Dai, and G. D. Liu, J. Mater. Chem. C **6**, 575 (2018).

[32] H. Huang, K. H. Jin, S. Zhang, and F. Liu, Nano Lett. **18**, 1972 (2018).

[33] M. Hirayama, S. Matsuishi, H. Hosono, and S. Murakami, Phys. Rev. X **8**, 031067 (2018).

[34] C. Park, S. W. Kim, and M. Yoon, Phys. Rev. Lett. **120**, 026401 (2018).

[35] S.-C. Zhu, L. Wang, J.-Y. Qu, J.-J. Wang, T. Frolov, X.-Q. Chen, and Q. Zhu, Phys. Rev. Mater. **3**, 024205 (2019).

[36] G. Kresse and D. Joubert, Phys. Rev. B **59**, 1758 (1999).

[37] P. E. Blochl, Phys. Rev. B **50**, 17953 (1994).

[38] J. P. Perdew, K. Burke, and M. Ernzerhof, Phys. Rev. Lett. **77**, 3865 (1996).

[39] S. L. Dudarev, G. A. Botton, S. Y. Savrasov, C. J. Humphreys, and A. P. Sutton, Phys. Rev. B **57**, 1505 (1998).

[40] N. Marzari and D. Vanderbilt, Phys. Rev. B **56**, 12847 (1997).

[41] M. P. López Sancho, J. M. López Sancho, and J. Rubio, J. Phys. F **15**, 851 (1985).

[42] Q. S. Wu, S. N. Zhang, H. F. Song, M. Troyer, and A. A. Soluyanov, Phys. Commun. **224**, 405 (2017).

[43] M. Jehle, H. Scherer, M. Wendorff, and C. Röhr, J. Solid State Chem. **182**, 1129 (2009).

[44] B. Bradlyn, L. Elcoro, J. Cano, M. Vergniory, Z. Wang *et al.*, Nature (London) **547**, 298 (2017).

[45] S. Nie, Y. Qian, J. Gao, Z. Fang, H. Weng, and Z. Wang, Phys. Rev. B **103**, 205133 (2021).

[46] J. Gao, Q. Wu, C. Persson, and Z. Wang, Comput. Phys. Commun. **261**, 107760 (2021).

[47] https://www.cryst.ehu.es/cgi-bin/cryst/programs/bandrep.pl.

[48] S. Liu, C. Wang, L. Liu, J. Choi, H.-J. Kim, Y. Jia, C. H. Park, and J. Cho, Phys. Rev. Lett. **125**, 187203 (2020).

[49] W. Li, H. Hu, and J.-H. Choi, Phys. Rev. B **103**, 195421 (2021).

[50] E. C. Stoner, Proc. R. Soc. London, Ser. A **169**, 339 (1939).

[51] T. Inoshita, N. Hamada, and H. Hosono, Phys. Rev. B **92**, 201109(R) (2015).

[52] C. J. Pickard and R. J. Needs, Phys. Rev. Lett. **107**, 087201 (2011).

[53] C. Liu, S. A. Nikolaev, W. Ren, and L. A. Burton, J. Mater. Chem. C **8**, 10551 (2020).

[54] J. Zhou, Y. P. Feng, and L. Shen, Phys. Rev. B **102**, 180407(R) (2020).

[55] T. J. Kim, H. Yoon, and M. J. Han, Phys. Rev. B **97**, 214431 (2018).

[56] H. Weng, Y. Liang, Q. Xu, R. Yu, Z. Fang, X. Dai, and Y. Kawazoe, Phys. Rev. B **92**, 045108 (2015).

[57] R. Yu, H. Weng, Z. Fang, X. Dai, and X. Hu, Phys. Rev. Lett. **115**, 036807 (2015).

[58] A. Yamakage, Y. Yamakawa, Y. Tanaka, and Y. Okamoto, J. Phys. Soc. Jpn. **85**, 013708 (2016).

[59] H. Huang, J. Liu, D. Vanderbilt, and W. Duan, Phys. Rev. B **93**, 201114(R) (2016).

[60] R. Wu and A. J. Freeman, Phys. Rev. B **47**, 3904 (1993).

[61] Y. Cheng, Y. Zheng, X. Huang, K. Zhong, Z. Chen, and Z. Huang, Rare Metals **31**, 130 (2012).

[62] X. Zhang, Z. Xiao, H. Lei, Y. Toda, S. Matsuishi, T. Kamiya, S. Ueda, and H. Hosono, Chem. Mater. **26**, 6638 (2014).

[63] S. H. Kang, J. Band, K. Chung, C. N. Nandadasa, G. Han *et al.*, Sci. Adv. **6**, eaba7416 (2020).

[64] H. Chen, W. Zhu, D. Xiao, and Z. Zhang, Phys. Rev. Lett. **107**, 056804 (2011).

[65] C. R. Rajamathi, U. Gupta, N. Kumar, H. Yang, and Y. Sun, Adv. Mater. **29**, 1606202 (2017).

[66] J. Li, H. Ma, Q. Xie, S. Feng, S. Ullah, R. Li, J. Dong, D. Li, Y. Li, and X. Chen, Sci. China Mater. **61**, 23 (2018).

[67] L. R. Wang, X. M. Zhang, W. Z. Meng, Y. Liu, X. F. Dai, and G. D. Liu, J. Mater. Chem. A **9**, 22453 (2021).